THERMAL EMISSION OF INTERMEDIATE MASS FRAGMENTS AND THE LIQUID-VAPOR PHASE TRANSITION

L. G. MORETTO, J. B. ELLIOTT, L. PHAIR, AND G. J. WOZNIAK

Nuclear Science Division, Lawrence Berkeley National Laboratory,
University of California, Berkeley, California, 94720

We study the origin of anomalous caloric curves and negative heat capacities in the liquid-gas coexistence region. Coexistence is described in terms of clusterization in the vapor according to Fisher's formula. Multifragmentation data are used to determine the liquid-vapor coexistence line. The phase diagram is obtained for the finite system and an extrapolation is made to infinite nuclear matter.

The nuclear thin skin is the basis of the liquid drop model, which manages to reproduce the binding energies of nuclei to within 1%. A similar leptodermous treatment of nuclear systems at $T > 0$ should lead to an equivalently good reproduction of nuclear thermodynamical properties.

The appearance of a vapor phase at $T > 0$ opens two complementary perspectives for the characterization of phase coexistence: the liquid perspective and the vapor perspective. From the liquid perspective, one can determine the caloric curve in terms of vaporization enthalpy. From the vapor perspective one considers the extent to which nucleons are aggregated into clusters, as an indicator of incipient liquid condensation.

In the first part of this presentation we take the liquid perspective and derive analytically the caloric curve and the (negative) heat capacity for a drop undergoing an isobaric phase transition. In the second part we take the vapor perspective and show that clusterization in the 3d Ising model can be accounted for in terms of the leptodermous expansion.

Recently, first order phase transitions in small systems were associated with anomalous convex intruders in the entropy versus energy curves, resulting in back-bendings in the caloric curve, and in negative heat capacities[1]. In the context of nuclear physics, the claim has been made of an empirical observation of these anomalies, such as negative heat capacities in nuclear systems[2].

In this section we investigate the role of varying potential energies ("ground states") with system size on caloric curves and negative heat capacities. Our study applies to leptodermous (thin skinned) van der Waals-like fluids and to models such as Ising, Potts, and lattice gas.

Consider a macroscopic drop of a van der Waals fluid with A constituents in equilibrium with its vapor. The vapor pressure p is given by

$$p \simeq p_o \exp\left(-\frac{\Delta H_m}{T}\right), \tag{1}$$

where ΔH_m is the molar vaporization enthalpy and ΔV_m is the molar change in volume. Equation (1) represents the p-T univariant line in the phase diagram for a drop of finite size where ΔH_m must be corrected for the surface energy of the drop[3]

$$p = p_0 \exp\left(-\frac{\Delta H_m^0}{T} + \frac{a_s}{A^{1/3}T}\right) = p_{\text{bulk}} \exp\left(\frac{a_s}{A^{1/3}T}\right). \tag{2}$$

where a_s is the surface energy coefficient. At constant T the vapor pressure increases with decreasing size of the drop (see Fig. 1).

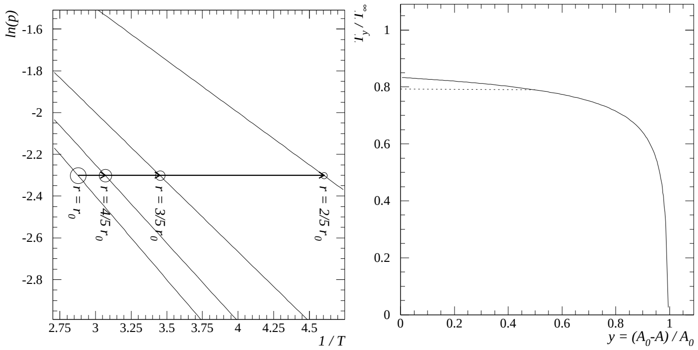

Figure 1. Left: the log of the saturated vapor pressure as a function of inverse temperature for different droplet radii. Arrows illustrate the path of evaporation at constant pressure. Right: The temperature as a function of droplet size for a drop evaporating at constant pressure (open boundary conditions). The solid line shows the case of a spherical drop, while the dotted line shows the case of a finite cubic lattice evolving as in Fig. 2 top.

Consider the case of isobaric evaporation of a drop starting from a drop with A_0 constituents and evaporating into a drop with $A < A_0$ constituents.

Let us define the drop size parameter $y = \frac{A_0 - A}{A_0}$. At constant pressure

$$p_0 \exp\left(-\frac{\Delta H_m^0}{T}\right) = p_0 \exp\left(-\frac{\Delta H_m(y)}{T_y}\right), \tag{3}$$

from which follows

$$\frac{T_y}{T_\infty} \simeq \frac{\Delta H_m(y)}{\Delta H_m^0} \simeq 1 - \frac{1}{A^{1/3}} \simeq 1 - \frac{1}{A_0^{1/3}(1-y)^{1/3}}. \tag{4}$$

A slight decrease in temperature is predicted as the drop evaporates isobarically, thus leading to a negative isobaric heat capacity in the coexistence region as illustrated in Fig. 1. As the drop is evaporating at constant pressure, the drop moves from one coexistence curve to another according to its decrease in radius, and thus to progressively lower temperatures. This slight effect is due not to an increase in surface since the drop surface of course diminishes as $A^{2/3}$, but to the slight increase of molar surface (see Fig. 2). Also, the formation of bubbles in the body of the drop is thermodynamically disfavored by the factor $f = \exp(-\gamma \Delta S/T)$ where ΔS is the surface of the bubble.

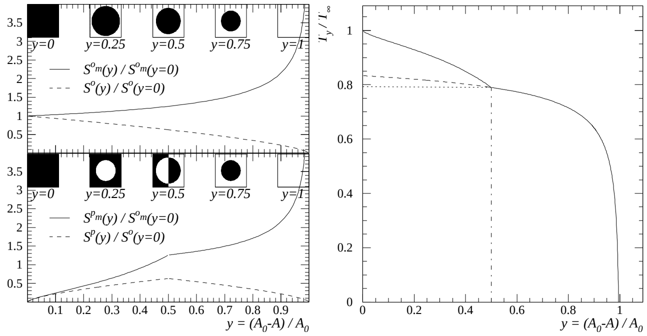

Figure 2. Left Top: The surface S^o (dashed) and molar surface S_m^o (solid) area of a drop for open boundary conditions normalized to their values at $y = 0$. Left Bottom: The surface S^p (dashed) and molar surface S_m^p (solid) area of a drop for periodic boundary conditions normalized to their values at $y = 0$. In-sets show the configurations at various values of y. Right: the temperature as a function of droplet size for a drop evaporating at constant pressure in a system with periodic boundary conditions. The solid line shows the case of a finite cubic lattice with periodic boundary conditions evolving as in Fig. 2 bottom, while the dotted line and the dashed line are the same as in Fig. 1 and the vertical dash-dotted line indicates the case of 50% lattice occupation.

Let us now move to the cases of lattice gas, Ising, and Potts models. We consider first an evaporating finite system in three dimensions of size

$A_0 = L^3$, with open boundary conditions. For maximal density at $T = 0$ (the ground state) $y = 0$ and the entire cubic lattice is filled. For decreasing densities, always at $T = 0$ a single cluster of minimum surface is present, which evolves from a cube to a sphere. The associated change in surface is shown in Fig. 2. The caloric curve from $y = 0$ to $y = 1/2$ is essentially flat like in the infinite system, and the heat capacity is trivially infinite.

The introduction of periodic boundary conditions rids the system of "dangling bonds." At $y = 0$, the lattice is filled with particles so that $\Delta H_m(0) = \Delta H_m^0$ characteristic of the infinite system. As y increases at fixed lattice size, a bubble develops in the cube and surface is rapidly created (see Fig. 2). The bubble develops since the periodic boundary conditions prevent evaporation from the surface. The bubble grows with increasing y until it touches the sides of the lattice. This occurs for $y \approx 1/2$. At nearly $y = 1/2$ and beyond, the "stable" configuration is a drop that eventually vanishes at $y = 1$. The change in surface associated with the range $0 \leq y \leq 1$ as well as the molar surface are shown in the bottom left panel of Fig. 2.

The evaporation enthalpy thus becomes

$$\Delta H_m(y) \simeq a_v \left(1 - \frac{y^{2/3}}{A_0^{1/3}\,(1-y)}\right) \tag{5}$$

from $y = 0$ to $y = 1/2$, and

$$\Delta H_m(y) \simeq a_v \left(1 - \frac{1}{A_0^{1/3}\,(1-y)^{1/3}}\right) \tag{6}$$

from $y = 1/2$ to $y = 1$. As a consequence, for periodic boundary conditions

$$\frac{T_y}{T_\infty} \simeq 1 - \frac{y^{2/3}}{A_0^{1/3}\,(1-y)} \tag{7}$$

from $y = 0$ to $y = 1/2$, while from $y = 1/2$ to $y = 1$ Eq. (4) holds.

The dramatic effect of periodic boundary conditions can be seen in Fig. 2. The temperature decreases substantially with increasing y, due to the fact that the molar enthalpy at $y = 0$ assumes its bulk value ΔH_m^0 and must meet the previous case of open boundary conditions for $y = 1/2$. This may well explain the calculated negative heat capacities reported in literature, as due to the unnatural choice of boundary conditions.

In the case of nuclei the quantity ΔH_m is determined by all the terms in the liquid drop model, which contribute to the mean binding energy per nucleon. One can immediately infer that when the binding energy per nucleon decreases with A, the heat capacity should be positive, and vice-versa. Thus, since the maximum binding energy per nucleon occurs at $A \sim 60$, negative heat capacities should be possible only for $A < 60$.

Explicitly,

$$C_p = \frac{\frac{(\Delta H_m(A))^2}{T}}{\frac{d\Delta H_m}{dA}}. \tag{8}$$

The derivative in the denominator can be evaluated approximately from the dependence on the binding energy per nucleon B upon the mass number $\frac{d\Delta H_m}{dA} = \frac{dB}{dA}$. The liquid drop model allows us to estimate such a derivative. From Fig. 3 it is apparent that the binding energy decreases with A for $A >\sim 60$. Consequently in all this region of A, positive specific heats should be expected. Only for $A <\sim 60$, negative specific heats are predicted.

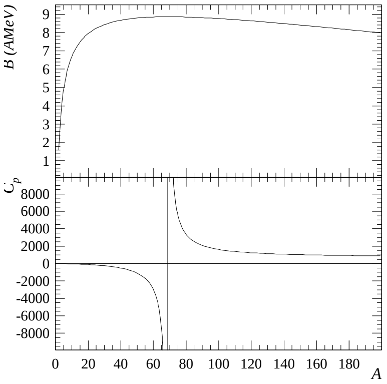

Figure 3. The binding energy of atomic nuclei (top) and the associated heat capacity (bottom).

This straightforward result based on elementary thermodynamics and ground state binding energies raises serious questions as to the meaning of the negative heat capacities claimed in large nuclear systems[2].

In multifragmentation, reducibility is the property that the probability of observing n-fragments of a given size is expressible in terms of an elementary one-fragment probability. Both binomial, and its limiting form, Poissonian reducibilities have been extensively documented experimentally for nuclear multifragmentation[4,5].

Thermal scaling is the linear dependence of the logarithm of the one-

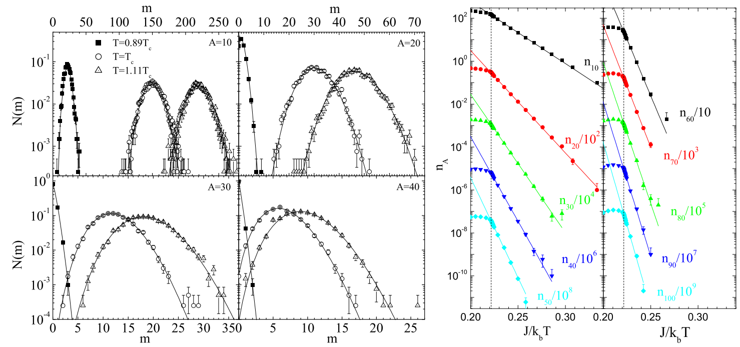

Figure 4. Left: The probability distributions for obtaining m fragments of size A at the three temperatures indicated. The solid lines are Poisson distributions with means given by the Monte Carlo data. Right: Arrhenius plots of the cluster distributions. The lines are fits of the form given in Eq. (9). The critical temperature is indicated by the dashed line.

fragment probability with $1/T$ (an Arrhenius plot) according to:

$$q_i = q_0 e^{-B_i/T} = q_0 e^{-c_0 A^\sigma/T} \tag{9}$$

where B_i is a "barrier" corresponding to the production process.

The combination of these two empirical features attests to a statistical mechanism of multifragmentation in general, and to liquid-vapor coexistence specifically[8].

In this light we analyze the Ising results in the same way as has been done with nuclear multifragmentation data[4,5]. Fig. 4 shows the multiplicity distributions for a sample of fragment sizes and temperatures. The solid lines represent Poisson distributions calculated from the corresponding mean multiplicities. The distributions are remarkably close to Poissonian for all masses and all temperatures below, at and above T_c.

If the fragment distributions exhibit thermal scaling, its Arrhenius plot should be linear. As shown in Fig. 4, this is the case over a wide range of temperatures ($0 < T < T_c$) and fragment sizes.

The features of reducibility and thermal scaling discussed above can be found united in Fisher's formula[6,7].

$$n_A(T) = q_0 A^{-\tau} \exp(\frac{c_0 A^\sigma}{T_c}) \exp(-\frac{c_0 A^\sigma}{T}) \tag{10}$$

where q_0 is a normalization constant, τ is a topological critical exponent, c_0 is the surface energy coefficient and $\varepsilon = (T_c - T)/T_c$. Therefore, a graph of the scaled cluster distributions ($n_A(T)A^\tau/q_0$) as a function of $\varepsilon A^\sigma/T$

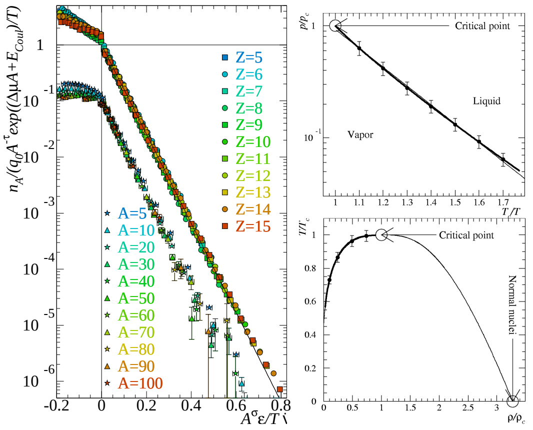

Figure 5. Left: the scaled yield distribution versus the scaled temperature for the ISiS data (upper) and $d = 3$ Ising model calculation (lower). Upper right: The reduced pressure-temperature phase diagram: Lower right: The reduced density-temperature phase diagram.

should collapse the distributions of all cluster sizes onto a single curve. This scaling behavior can clearly be seen in Fig. 5.

The ISiS data sets

The ISiS charge yields from AGS experiment of 8 GeV/c π + Au fragmentation data were fit to the following modified form of Eq. (10) which incorporates the Coulomb. The scaled data shown in Fig. 5 collapse to a single line over six orders of magnitude. This line is the liquid to vapor phase coexistence line in excited nuclei.

Fisher's model assumes that the non-ideal vapor can be approximated by an ideal gas of clusters. Accordingly, the total pressure is the sum of their partial pressures: $p/T = \sum n_A$. The resulting p, T diagram is given in Fig. 5.

Fitting the coexistence line $p/p_c = \exp(\Delta H/T_c(1 - T_c/T))$ which describes many fluids gives $\Delta H = 26 \pm 1$ MeV from which $\Delta E \approx 15$ AMeV, remarkably close to the nuclear bulk energy coefficient.

The system's density can be found from $\rho = \sum A n_A$ as shown in Fig. 5. Following Guggenheim[9]:

$$\frac{\rho_{l,v}}{\rho_c} = 1 + b_1(1 - \frac{T}{T_c}) \pm b_2(1 - \frac{T}{T_c})^{1/3}. \tag{11}$$

Fitting the coexistence curve from the ISiS E900a data with Eq. (11) one obtains an estimate of the full ρ_v branch of the coexistence curve and changing the sign of b_2 gives the full ρ_l branch of the coexistence curve of finite neutral nuclear matter. The critical density is found to be $\rho_c \sim 0.3\rho_0$.

The EOS data sets

The EOS Collaboration has collected data for the reverse kinematics reactions 1.0 *A*GeV Au+C, 1.0 *A*GeV La+C and 1.0 *A*GeV Kr+C[10,11].

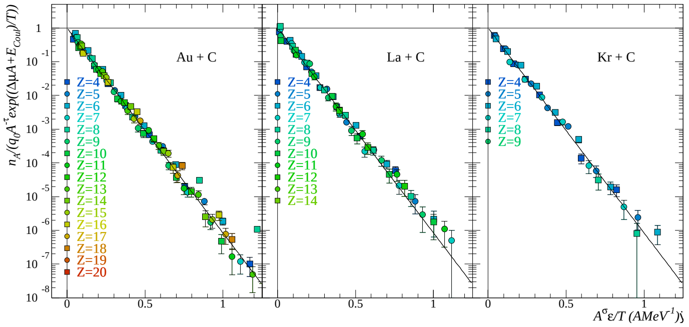

Figure 6. The scaled yield distribution versus the scaled temperature for the gold, lanthanum and krypton systems. The solid line has a slope of c_0.

Fig. 6 shows the Fisher plot of fragment mass yield distribution scaled by the power law pre-factor, the chemical potential and Coulomb terms. The scaled data for all three systems collapse onto a single line over several orders of magnitude. This collapse provides direct evidence for a liquid to vapor phase transition in excited nuclei.

The p-T and T-ρ coexistence curves can be determined from this analysis by transforming the information in Fig. 6 into the phase diagrams in Fig. 7. From these it is possible to make an estimate of the bulk binding energy of nuclear matter and the $\Delta E/A \approx$14 MeV, close to the nuclear bulk energy coefficient of 15.5 MeV.

Finite size effects are paramount in nuclei. The binding energy per nucleon decreases from the $\sim$ 15.5 *A*MeV of nuclear matter to about 8 *A*MeV for typical nuclei.

We can expect that such a drastic reduction affects the critical temperature as well. The Ising model can be used again as a simple testing ground. If a finite system is considered (no periodic boundary conditions) a surface is generated with the attendant surface energy. This allows us to write a "liquid drop" formula for the Ising model: $E = a_V A + a_S A^{2/3}$.

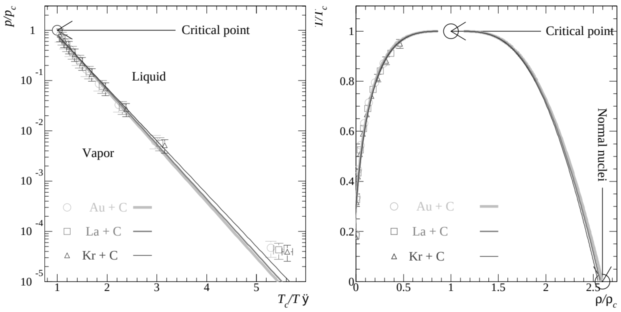

Figure 7. EOS data results. Left: The reduced pressure-temperature phase diagram. The lines show fits to the Clausius-Clapeyron equation. Right: the reduced density-temperature phase diagram. The lines are a fit to and reflection of Guggenheim's equation.

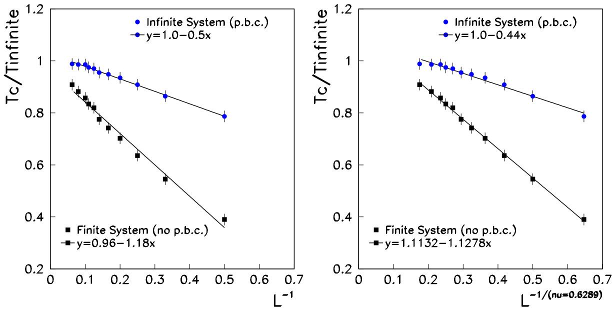

Figure 8. Left: the naive estimate of finite size scaling. Right: a more sophisticated estimate of finite size scaling. The data points and fits on the bottom of both figures show the results for lattices with open boundary conditions (no p.b.c.) and more closely represent the case of finite systems like nuclei.

We now determine the critical temperature for various sizes (lattices) and check its dependence on the lattice size (see Fig. 8). For a finite system all the quantities with the dimension of energy should scale with the binding energy per site corrected for the surface energy

$$\frac{T_c^{A_0}}{T_c^{\infty}} = \frac{a_V A_0 + a_S A_0^{2/3}}{a_V A_0} = 1 - \frac{1}{A_0^{1/3}} = 1 - \frac{1}{L} \tag{12}$$

where A_0 is the number of sites in the lattice and L is the linear lattice side. As we can see in Fig. 8, this scaling works quite well.

The result of this exercise shows that the critical temperature of infinite nuclear matter can be obtained in a similar way. In each of the three EOS reactions, remnants of different sizes make a good range of A_0 accessible.

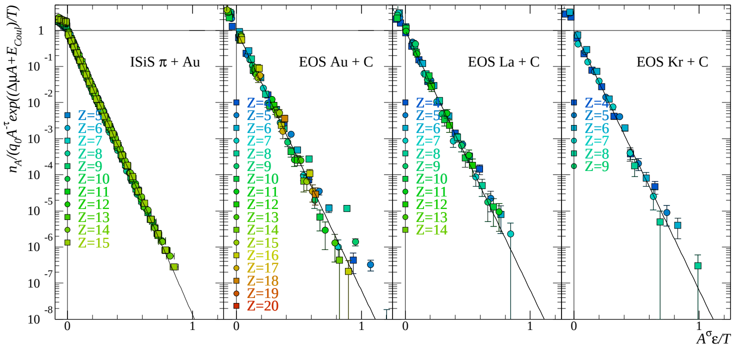

Figure 9. Fisher scaling and finite size scaling analysis of the ISiS and EOS data sets.

The preliminary results are shown in Fig. 9. The extracted values for the critical temperature of infinite nuclear matter are ∼ 13.6 MeV from the ISiS data and ∼ 12.9 MeV from the EOS data. These values agree with theoretical estimates of the critical temperature of bulk nuclear matter.

We thank Prof. C.M. Mader, Prof. R. Ghetti and Prof. J. Helgesson for their input and Ising model calculations and we acknowledge the experimental efforts of the ISiS and EOS collaborations. This work was supported by the US Department of Energy.

References

1. D. H. E. Gross, Phys. Rep. **279**, 119 (1997).
2. M. D'Agostino *et al.*, Phys. Lett. B, **473**, 219 (2000).
3. L. Rayleigh, Phil. Mag. **34**, 94 (1917).
4. L. G. Moretto, *et al.*, Phys. Rep. **287**, 249 (1997).
5. L. Beaulieu *et al.*, Phys. Rev. Lett. **81**, 770 (1998).
6. M. E. Fisher, Physics **3**, 255 (1967).
7. M. E. Fisher, Rep. Prog. Phys. **30**, 615 (1969).
8. J. B. Elliott *et al.*, Phys. Rev. Lett. **85**, 1194 (2000).
9. E.A. Guggenheim, J. Chem. Phys., **13**, 253 (1945).
10. J. A. Hauger *et al.*, Phys. Rev. C **57**, 764 (1998)
11. J. A. Hauger *et al.*, Phys. Rev. C **62**, 024626 (2000).